Landslides in Padang Pariaman during the 2009 Padang Earthquake: Field Survey and GIS Analysis

Siau Chen CHIAN
National University of Singapore, Singapore
Phone: +65-6516-4729
Fax: +65-6779-1635
Email: sc.chian@nus.edu.sg

Sean WILKINSON
Newcastle University, United Kingdom

Abstract

The M_w 7.6 Sumatra earthquake that occurred on 30th September 2009 resulted in very large landslides in the regency of Padang Pariaman, in West Sumatra. The UK based Earthquake Engineering Field Investigation Team (EEFIT) was dispatched to conduct a field survey of the effects of the earthquake, including the landslides that affected the region. As part of the mission, the feasibility of using remote sensing to determine vulnerability to landslides was assessed. Comparison of coordinates between the collected GPS readings in the field, ASTER and Google^{TM} Earth DEMs and SPOT-5 satellite imagery showed reasonable spatial and elevation differences which indicates the suitability of remote sensing for landslide hazard assessments. Deterministic slope stability model analysis with SINMAP also indicated high susceptibility of slope instability at these landslide sites. These locations however, were demarcated as moderate risk regions in the local landslide hazard map. Considering the high lethality of these landslides, this underestimate of the risk is a strong argument for a review of landslide risks using a methodology that considers the combined effects of earthquake and rainfall as evident in this earthquake event.

Keywords: Padang Pariaman regency, landslide; earthquake, rainfall, field survey, SINMAP, hazard map

Introduction

A major earthquake, with a magnitude of M_w 7.6 occurred off the coast of West Sumatra on the 30th of September 2009 at 17:16 local time (10:16 UTC). The focus was located at 0.725°S, 99.856°E at a depth of 81 km (USGS 2010a). The approximate distances of the epicentre from the cities of Pariaman (i.e. Kota Pariaman) and Padang (Kota Padang) are 30 km and 60 km respectively. This main shock was followed the next day at 08:52 local time (01:52 UTC) by an aftershock, with magnitude M_w 6.6, focal depth of 15 km and an epicentre located inland, 250 km SSE from Pariaman (see Fig. 1). The M_w 7.6 intermediate depth earthquake was triggered by an oblique-thrust fault near a long undersea subduction fault interface between the Australian and Sunda plates, while the M_w 6.6 occurred due to a dextral (right-lateral) strike-slip movement at the nearby Great Sumatran fault (USGS 2010a,b) The epicentre of the M_w 7.6 earthquake occurred in the same tectonic region as the great M_w 9.1 Sumatra-Andaman earthquake in 2004 that generated a tsunami resulting in 228,700 deaths in 14 countries (EM-DAT 2013).

[Insert Fig. 1 about here]

Sumatra's Historical Seismicity and Landslide Susceptibility

The island of Sumatra is located adjacent to the Pacific Ring of Fire, and the nearby active tectonic fault boundaries are the site of many large earthquakes. The seismicity in the region is determined mainly by the subduction of the Australian plate beneath the Sunda plate. The subduction zone between these tectonic plates lies on the western side of Sumatra, forming the Sunda trench. This long undersea subduction zone is known for producing mega-thrust earthquakes such as the M_w 8.8-9.2 in 1833, the Mw 8.3-8.5 in 1861, the M_w 9.1 in December 2004, the M_w 8.7 in March 2005 and the M_w 8.4 in September 2007 (Irsyam *et al.* 2008). The inland Great Sumatran fault lies parallel to the subduction zone and is highly segmented with majority of the segments less than 100 km long (Natawidjaja 2002).

The geology of Padang city is characterized by the flat coastal plain and volcanic mountainous terrain inland. The coastal area is mainly made up of young alluvium sediments, while the mountains are comprised of quaternary volcanic sediments which have been exposed to long-term erosion (Petersen *et al.* 2007). Many of these mountainous areas are populated due to their suitability for agriculture; however, these steep slopes accompanied with loose weathered sediments are very prone to landslides especially in the wet months of January and August. A potential landslide hazard map has been produced by the Indonesian National Board for Disaster Management, BNPB and is shown in Fig. 2.

[Insert Fig. 2 about here]

The 30th September 2009 Earthquake

The epicentre of the intermediate depth M_w 7.6 earthquake is situated in the sea between Siberut Island and Pariaman city. It is 60 km northwest of Padang city, the capital of West Sumatra with a population of around 900,000. As a result of this earthquake, 379,201 buildings were heavily damaged, with 3,515 injury cases and 1,117 fatalities (BNPB 2009). In view of the significance of the event, the UK Earthquake Field Investigation Team (EEFIT) visited the affected regions to study the damage resulting from the earthquake. Fig. 3 indicates the location of major landslides and the number of damaged buildings, injuries and fatalities in the 11 affected regencies and municipalities. The distribution of damage as shown in the figure was in agreement with the degree of shaking based on the Modified Mercalli Intensity (MMI), with districts nearer to the earthquake epicentre suffering heavier losses. Numerous large scale landslides followed as a result of the strong shaking and heavy rainfall that preceded the earthquake as evident in the rainfall measurements in Fig. 4. Almost a third of the total fatalities (321 out of the 1,117) were attributed to landslides that occurred in Padang Pariaman, one of the 4 regencies of West Sumatra province seriously affected by the earthquake (BNPB 2009). Such a high number of landslide-related fatalities is strong evidence for the need of further studies on landslide susceptibility in the region. This paper covers the

investigation of landslides induced by the earthquake. Other findings of the reconnaissance can be obtained from Wilkinson *et al.* (2009).

[Insert Fig.3 and 4 about here]

Post Earthquake Field Survey on Landslides

Based on a report by OCHA (2009), more than 1000 landslides occurred in Padang Pariaman regency. Some of these major landslides were visited during the EEFIT reconnaissance. These landslides were particularly clustered in the Gunung Tigo highlands between Padang Pariaman and Agam regencies as well as in Kota Padang (Padang municipality) and Solok district as indicated in Fig. 3. Most casualties were in rural Padang Pariaman and Agam, which are both located adjacent to two large volcanoes, Mount Tandikat (2,438 m) and Mount Singgalang (2,877 m). Due to the fertility of the land, the majority of rural communities in West Sumatra were situated in agriculturally-intensive villages near the foot of volcanoes. Figs. 5 and 6 show one of the sections of the landslide affecting the Pulau Air village and Cumanak village respectively. Both landslides were sited in one of the worst affected areas of Nagari Tandikek. Landslides in Nagari Tandikek resulted in 252 fatalities, of which 145 bodies were not recovered (BNPB 2009). Two villages, Pulau Air and Cumanak (casualties of 45 and 75 respectively) were completely destroyed by these two landslides. Roads in the path of the landslides were buried restricting access to the affected areas and hindered rescue operations.

[Insert Fig. 5 and 6 about here]

Despite the lower population density in these mountainous regions as compared to the urban city areas, the high number of fatalities was partly due to a large gathering of villagers attending a wedding ceremony in Cumanak Village, where a major landslide occurred. Initially meant to be a blissful occasion, this turned tragic when the combined contributions of heavy rainfall and strong earthquake shaking accompanied with a large gathering of people provided 'perfect' conditions for a landslide with high lethality. Many of the surviving local residents, who had been at work in the city, lost their family members. EEFIT conducted interviews with the survivors, one of whom had lost all 38 family members in the landslide. The EEFIT team was also informed by the locals that there had not been a great deal of rain in the weeks preceding the earthquake, however, heavy rain occurred the night before and in the morning of the day of the earthquake. This is verified with the rainfall intensity estimated by the Tropical Rainfall Measurement Mission (TRMM) of the National Aeronautics and Space Administration (NASA) and the Japan Aerospace Exploration Agency (JAXA) as shown in Fig. 4. Significant reduction of the soil's shear strength due to high saturation level from the rainfall infiltration and excess pore pressure build-up from the strong shaking could have led to slope instability of many of these previously stable slopes. Due to its scale and importance, this particular landslide would constitute one of the landslides studied in this paper.

At the time of the reconnaissance, Landslide *I* (see Fig. 5) at Pulau Air village was accessible via car. The height of the scarp and runoff distance was measured as 65 m and 230 m respectively. The characteristics of the landslide measured using GPS receivers and laser measurement devices were as follows: elevation of scarp (247 m), elevation of base of scarp (182 m), landslide length (230 m), maximum landslide width (120 m), average landslide thickness

(5 m), and approximate maximum slope angle (45°). The estimated landslide velocity was 49 m/s following Slingerland and Voight (1979). As the landslide resembles a quarter ellipsoid-shaped mass with its maximum width coinciding with its toe, the landslide volume was approximated to be 10,210 m^3 based on the formula by Cruden and Varnes (1996). Landslide *II* (See Fig. 6) at Cumanak Village had one of the highest number of casualties (total 75; 34 found and 41 not found). The site could only be accessed by foot through a damaged pedestrian suspension bridge across a river stream (this bridge had been damaged by the landslide). Using measurements from satellite images, the extent of the landslide was approximately 2 km long and up to 1.5 km wide.

Feasibility of Remote Sensing for Landslide Analysis

Apart from visual investigations of the landslides, the authors were interested to determine the reliability and feasibility of using remote sensing for landslide assessments. This is in view of the large extent of earthquake induced landslides during the 2008 Wenchuan earthquake in China (Free *et al.* 2008). The authors therefore undertook the risky task of ascending the boundaries of the two landslides in order to accurately determine their geographic position. Many of these areas near the edge of the failed slope were unstable with large tension cracks hidden within the dense vegetation in the tropical forest setting. Matters were made worst with heavy rain occurring when the authors were near the summit of a major landslide (Landslide *II*). From the authors' experience, it is evident that field demarcation of landslide boundaries is a difficult and sometimes hazardous task and remote sensing would present a more feasible means to study landslides especially those covering a wide area. However, before detailed analysis with remote sensing techniques can be conducted, the accuracy of data sources needs to be assessed. The four sources of data applied in the study are: a) the Global Positioning System (GPS) survey readings collected in the field, b) the Advanced Spaceborne Thermal Emission and Reflection Radiometer (ASTER) Digital Elevation Model (DEM), c) the Satellite Pour L' Observation de la Terre (SPOT) post-disaster satellite imagery acquired by the Centre for Remote Imaging, Sensing and Processing at the National University of Singapore (CRISP NUS), and d) the Google™ Earth base. The on-site GPS survey readings were collected via a TOPCON GPS hand-held receiver electronically based on the average coordinates from a least three strong signal-emitting satellites in the vicinity. The differences between the on-site coordinates and elevations collected by the hand-held GPS receiver for each survey point were less than 0.23 seconds in the longitudinal and latitudinal coordinates and 6.9 m in elevation. The ASTER DEM has a spatial resolution of approximately 30 m. The SPOT-5 satellite imagery has a spatial resolution of 10 m. The Google™ Earth base is constructed with SRTM DEM of assumed 90m in spatial resolution.

[Insert Fig. 7a and 7b about here]

Landslide *I* (a small landslide) and Landslide *II* (a large scale landslide) as mentioned earlier were selected to 1) assess repeatability, 2) ascertain any influence the size of landslide may have on the deviation in coordinates between data sources, and 3) determine the range of difficulties likely to be encountered when collecting such field data. A number of points along the boundaries of the two landslides were selected for the comparison of aerial coordinates and elevation between the different data sources. Points on the boundaries of these landslides were taken where there was obvious change in alignment (e.g. concave or convex intersections at plan view) as shown in Fig. 7. Tables 1 and 2 provide the coordinates of these points for the two landslides. In these tables, the GPS survey

horizontal coordinates (latitude and longitude) and elevation readings obtained directly from the GPS hand-held receiver at the location of the landslide boundary points are presented. SPOT-5 horizontal coordinates of these points are taken from a geographic information system software, ArcGIS after overlaying the imagery onto the datum projection with the accompanying reference coordinates of the imagery. Due to the nature of the satellite imagery, the elevation of these points in the SPOT-5 imagery is not available; however, by relying on the horizontal coordinates from the SPOT-5 imagery, the elevation of these boundary points can be obtained from the ASTER and Google™ Earth DEMs. The coordinates (latitude, longitude and elevation) from these data sources is thereafter compared with their root mean square (RMS) as shown in Tables 1 and 2. The root mean square computation is as shown in Eq. 1. The maximum difference with RMS at the far right column is computed by taking the largest difference of the data sources and the RMS (i.e. 240 m - 220.8 m = 19.2 m for the elevation RMS difference at Boundary Point A).

$$x_{RMS} = \sqrt{\frac{1}{n}(x_1^{\,2} + x_2^{\,2} + \ldots + x_n^{\,2})} \tag{1}$$

where x is the coordinate (latitude, longitude or elevation).

Table 1 Coordinates of the boundaries of Landslide *I* from GPS Survey, SPOT-5 Imagery, ASTER DEM and Google™ Earth

Boundary Point	GPS Survey	SPOT-5 Imagery	ASTER DEM	Google™ Earth	Root Mean Square (RMS)	Max Difference with RMS
A	00°29'49.14"S	00°29'48.74"S	Based on Coordinates		00°29'48.94"S	0.20" (6.2 m)
	100°14'28.09"E	100°14'27.36"E	from SPOT-5 Imagery		100°14'27.73"E	0.37" (11.4 m)
	240.000 m	-	205 m	216 m	220.8 m	19.2 m
B	00°29'51.22"S	00°29'51.05"S	Based on Coordinates		00°29'51.13"S	0.10" (3.1 m)
	100°14'25.51"E	100°14'25.19"E	from SPOT-5 Imagery		100°14'25.29"E	0.22" (6.8 m)
	186.605 m	-	201 m	198 m	195.3 m	8.7 m
C	00°29'52.14"S	00°29'52.04"S	Based on Coordinates		00°29'52.09"S	0.05" (1.5 m)
	100°14'25.37"E	100°14'25.07"E	from SPOT-5 Imagery		100°14'25.22"E	0.15" (4.6 m)
	200.216 m	-	200 m	192 m	197.4 m	5.4 m
D	00°29'54.08"S	00°29'53.83"S	Based on Coordinates		00°29'53.96"S	0.13" (4.0 m)
	100°14'23.96"E	100°14'23.55"E	from SPOT-5 Imagery		100°14'23.76"E	0.21" (6.5 m)
	198.397 m	-	193 m	184 m	191.9 m	7.9 m
E	00°29'56.14"S	00°29'56.11"S	Based on Coordinates		00°29'56.13"S	0.02" (0.6 m)
	100°14'25.08"E	100°14'24.83"E	from SPOT-5 Imagery		100°14'24.96"E	0.13" (4.0 m)
	187.860 m	-	182 m	180 m	183.3 m	4.5 m
F	00°29'55.01"S	00°29'54.74"S	Based on Coordinates		00°29'54.88"S	0.14" (4.3 m)
	100°14'27.65"E	100°14'27.04"E	from SPOT-5 Imagery		100°14'27.35"E	0.31" (9.6 m)
	184.767 m	-	184 m	184 m	184.3 m	0.5 m
G	00°29'52.07"S	00°29'51.97"S	Based on Coordinates		00°29'52.02"S	0.05" (1.5 m)
	100°14'28.04"E	100°14'27.54"E	from SPOT-5 Imagery		100°14'27.79"E	0.25" (7.7 m)
	187.731 m	-	201 m	198 m	195.7 m	7.9 m

Table 1 refers to the coordinates of Landslide *I* as shown in Fig. 7a. The results of the computations indicate a low maximum difference with RMS (i.e. max. difference in coordinate between all data sources and their RMS) of 0.37 arc seconds (about 11.4 m) or less for the horizontal coordinates (longitude and latitude). The maximum difference with RMS in elevation between the GPS survey, Google™ Earth and the ASTER DEM displayed reasonable difference of between 0.5m and 19.2m. This range is in the same order as the height of the vegetation within the

survey region (the tree height was estimated to be between 5 and 15 m). These results demonstrate an acceptable level of accuracy within the applied remote sensing technologies for landslide hazard assessments within the region.

Table 2 Coordinates of the boundaries of Landslide *II* from GPS Survey, SPOT-5 Imagery, ASTER DEM and Google™ Earth

Boundary Point	GPS Survey	SPOT-5 Imagery	ASTER DEM	Google™ Earth	Root Mean Square (RMS)	Max Difference with RMS
a	00°29'31.07"S	00°29'31.53"S	Based on Coordinates		00°29'31.30"S	0.23" (7.1 m)
	100°14'18.24"E	100°14'18.01"E	from SPOT-5 Imagery		100°14'18.13"E	0.12" (3.7 m)
	194.951 m	-	192 m	194 m	193.7 m	1.7 m
b	00°29'29.42"S	00°29'29.21"S	Based on Coordinates		00°29'29.32"S	0.11" (3.4 m)
	100°14'17.32"E	100°14'17.43"E	from SPOT-5 Imagery		100°14'17.38"E	0.06" (1.8 m)
	198.789 m	-	197 m	199 m	198.3 m	1.3 m
c	00°29'30.28"S	00°29'30.07"S	Based on Coordinates		00°29'30.18"S	0.11" (3.4 m)
	100°14'15.18"E	100°14'15.15"E	from SPOT-5 Imagery		100°14'15.17"E	0.02" (0.6 m)
	197.319 m	-	203 m	207 m	202.5 m	5.2 m
d	00°29'28.33"S	00°29'28.25"S	Based on Coordinates		00°29'28.29"S	0.04" (1.2 m)
	100°14'14.12"E	100°14'13.89"E	from SPOT-5 Imagery		100°14'14.01"E	0.12" (3.7 m)
	207.440 m	-	208 m	214 m	209.8 m	4.2 m
e	00°29'27.36"S	00°29'27.21"S	Based on Coordinates		00°29'27.29"S	0.08" (2.5 m)
	100°14'10.20"E	100°14'10.24"E	from SPOT-5 Imagery		100°14'10.22"E	0.02" (0.6 m)
	219.944 m	-	230 m	234 m	228.1 m	8.1 m
f	00°29'26.56"S	00°29'26.29"S	Based on Coordinates		00°29'26.43"S	0.14" (4.3 m)
	100°14'08.96"E	100°14'08.95"E	from SPOT-5 Imagery		100°14'08.96"E	0.01" (0.3 m)
	254.278 m	-	235 m	241 m	243.6 m	10.7 m
g	00°29'26.97"S	00°29'26.80"S	Based on Coordinates		00°29'26.89"S	0.09" (2.8 m)
	100°14'07.65"E	100°14'07.58"E	from SPOT-5 Imagery		100°14'07.62"E	0.04" (1.2 m)
	225.549 m	-	249 m	251 m	242.1 m	16.6 m
h	00°29'26.21"S	00°29'26.06"S	Based on Coordinates		00°29'26.14"S	0.08" (2.5 m)
	100°14'07.26"E	100°14'07.18"E	from SPOT-5 Imagery		100°14'07.22"E	0.04" (1.2 m)
	218.160 m	-	251 m	255 m	242.0 m	23.8 m
i	00°29'25.05"S	00°29'25.00"S	Based on Coordinates		00°29'25.03"S	0.03" (0.9 m)
	100°14'06.56"E	100°14'06.59"E	from SPOT-5 Imagery		100°14'06.58"E	0.02" (0.6 m)
	239.167 m	-	250 m	258 m	249.2 m	10.0 m
j	00°29'24.80"S	00°29'24.59"S	Based on Coordinates		00°29'24.70"S	0.11" (3.4 m)
	100°14'04.38"E	100°14'04.39"E	from SPOT-5 Imagery		100°14'04.39"E	0.01" (0.3 m)
	246.621 m	-	284 m	276 m	269.4 m	22.7 m
k	00°29'21.59"S	00°29'21.23"S	Based on Coordinates		00°29'21.41"S	0.18" (5.5 m)
	100°14'02.21"E	100°14'02.17"E	from SPOT-5 Imagery		100°14'02.19"E	0.02" (0.6 m)
	293.668 m	-	283 m	291 m	289.3 m	6.3 m
l	00°29'20.58"S	00°29'20.81"S	Based on Coordinates		00°29'20.70"S	0.12" (3.7 m)
	100°14'02.67"E	100°14'02.74"E	from SPOT-5 Imagery		100°14'02.71"E	0.04" (1.2 m)
	233.040 m	-	272 m	285 m	264.3 m	31.2 m
m	00°29'20.26"S	00°29'19.79"S	Based on Coordinates		00°29'20.03"S	0.24" (7.4 m)
	100°14'02.14"E	100°14'02.13"E	from SPOT-5 Imagery		100°14'02.14"E	0.01" (0.3 m)
	242.925 m	-	279 m	287 m	270.3 m	27.4 m
n	00°29'17.91"S	00°29'17.96"S	Based on Coordinates		00°29'17.94"S	0.03" (0.9 m)
	100°14'02.90"E	100°14'02.89"E	from SPOT-5 Imagery		100°14'02.90"E	0.01" (0.3 m)
	270.278 m	-	283 m	282 m	278.5 m	8.2 m
o	00°29'18.00"S	00°29'18.00"S	Based on Coordinates		00°29'18.00"S	0.00" (0.0 m)
	100°14'04.16"E	100°14'04.16"E	from SPOT-5 Imagery		100°14'04.16"E	0.00" (0.0 m)
	270.417 m	-	276 m	276 m	274.2 m	3.7 m
p	00°29'19.14"S	00°29'19.34"S	Based on Coordinates		00°29'19.24"S	0.10" (3.1 m)
	100°14'05.18"E	100°14'05.18"E	from SPOT-5 Imagery		100°14'05.18"E	0.00" (0.0 m)
	298.097 m	-	259 m	266 m	274.9 m	23.2 m

q	00°29'20.17"S	00°29'20.26"S	Based on Coordinates		00°29'20.22"S	0.05" (1.5 m)
	100°14'06.22"E	100°14'06.17"E	from SPOT-5 Imagery		100°14'06.20"E	0.03" (0.9 m)
	238.157 m	-	249 m	259 m	248.9 m	10.7 m
r	00°29'21.65"S	00°29'21.66"S	Based on Coordinates		00°29'21.66"S	0.01" (0.3 m)
	100°14'07.61"E	100°14'07.59"E	from SPOT-5 Imagery		100°14'07.60"E	0.01" (0.3 m)
	240.653 m	-	244 m	251 m	245.3 m	5.7 m
s	00°29'22.39"S	00°29'22.32"S	Based on Coordinates		00°29'22.36"S	0.04" (1.2 m)
	100°14'09.30"E	100°14'09.33"E	from SPOT-5 Imagery		100°14'09.32"E	0.02" (0.6 m)
	210.772 m	-	234 m	248 m	231.4 m	20.7 m
t	00°29'23.07"S	00°29'23.09"S	Based on Coordinates		00°29'23.08"S	0.01" (0.3 m)
	100°14'10.55"E	100°14'10.53"E	from SPOT-5 Imagery		100°14'10.54"E	0.01" (0.3 m)
	185.987 m	-	231 m	229 m	216.3 m	30.3 m
u	00°29'21.58"S	00°29'21.37"S	Based on Coordinates		00°29'21.48"S	0.11" (3.4 m)
	100°14'12.07"E	100°14'12.19"E	from SPOT-5 Imagery		100°14'12.13"E	0.06" (1.8 m)
	183.882 m	-	217 m	216 m	206.2 m	22.3 m
v	00°29'23.59"S	00°29'23.56"S	Based on Coordinates		00°29'23.58"S	0.02" (0.6 m)
	100°14'12.24"E	100°14'12.22"E	from SPOT-5 Imagery		100°14'12.23"E	0.01" (0.3 m)
	255.965 m	-	220 m	219 m	232.3 m	23.7 m
w	00°29'24.43"S	00°29'24.39"S	Based on Coordinates		00°29'24.41"S	0.02" (0.6 m)
	100°14'13.24"E	100°14'13.17"E	from SPOT-5 Imagery		100°14'13.21"E	0.04" (1.2 m)
	254.765 m	-	216 m	215 m	229.3 m	25.4 m
x	00°29'25.21"S	00°29'25.05"S	Based on Coordinates		00°29'25.13"S	0.08" (2.5 m)
	100°14'14.70"E	100°14'14.24"E	from SPOT-5 Imagery		100°14'14.47"E	0.23" (4.6 m)
	249.344 m	-	211 m	248 m	236.8 m	25.8 m

The data in Table 2 shows the measurements for part of Landslide *II* in Fig. 7b. Despite the larger extent of Landslide *II* in comparison to Landslide *I*, the maximum difference with RMS in the longitude and latitude of Landslide *II* (approximately 0.24 arc seconds or 7.3 m) obtained from the SPOT-5 imagery and the GPS survey records is similar to Landslide *I*. This indicates that the accuracy of the coordinates from the satellite imagery is independent of the scale of the landslide.

The maximum difference in the RMS readings of elevation between the GPS survey, Google™ Earth and the ASTER DEM are larger than those of Landslide *I* (31.2 m in Landslide *II* versus 19.2 m in Landslide *I*). Although most of the differences between the GPS survey and the remotely sensed data are less than the tree height, a few points are greater. It is believed that the discrepancies between the data sources are probably due to the GPS readings being computed as the average of only 3 epochs. The difficulty in surveying such a large and potentially dangerous landslide, thick forest cover and lack of available time in the field meant it was not possible to take more readings to obtain a better estimate of the elevation. In order to further substantiate the suitability of remote sensing for landslide hazard assessment, a deterministic slope stability analysis model (SINMAP) is conducted and the methodology and results are discussed in the following section.

Deterministic Analysis of Landslides

Methodology

The SINMAP (Stability Index MAPping) model based on Hammond *et al.* (1992) is a slope stability predictive tool that combines a mechanistic infinite slope stability model with hydrology. In the geotechnical aspect, the model balances the destabilising components of gravity forces on the soil and the restoring components of friction and

cohesion on an assumed infinite failure plane parallel to the ground surface to derive the factor of safety (FS) as shown in Eq. 2.

$$FS = \frac{C_r + C_s + cos^2\theta[\rho_s\, g\,(D - D_w) + (\rho_s\, g - \rho_w g)\, D_w]tan\Phi}{D\rho_s\, g\, sin\theta\, cos\theta} \tag{2}$$

where C_r is the root cohesion in N/m^2, C_s is the soil cohesion, θ is the slope angle, ρ_s is the saturated soil density, ρ_w is the density of water, g is the gravitational acceleration of 9.81 m/s^2, D is the vertical soil depth, D_w is vertical height of the water table in the soil layer, and Φ is the internal friction angle of the soil. The above equation was subsequently adapted by Pack *et al.* (2005) to develop a factor of safety with dimensionless parameters encompassing hydrologic aspects as shown in Eq. 3.

$$FS = \frac{C + cos\theta(1 - wr)tan\Phi}{sin\theta} \tag{3}$$

where the dimensionless cohesion *C*, wetness index *w* and density ratio *r* are:

$$C = \frac{C_r + C_s}{h\,\rho_s\, g} = \frac{C_r + C_s}{D\, cos\theta\, \rho_s\, g} \tag{4}$$

$$w = \frac{D_w}{D} = \min\left(\frac{R\,a}{T\, sin\theta}, 1\right) \tag{5}$$

$$r = \frac{\rho_w}{\rho_s} \tag{6}$$

The *R*, *T* and *a* terms in Eq. 5 are the recharge, soil's transmissivity and specific catchment area respectively. The specific catchment area is defined as the contributing slope area per unit contour length in m^2/m. In order to consider the uncertainties of the parameters in Eq. 3, the lowest factor of safety (FS_{min}) based on the permutations of lower and upper values of cohesion [*C*], topographic relative wetness [*T/R*] and friction angle [Φ] are taken to be the stability index (SI) for a site. An SI map can therefore be produced for a region. Areas of SI value lower than 1 (denoted as red in an SI map) are deemed to be susceptible to landslide based on the given conditions of the soil as specified in the parameters. Further details of the development of the SINMAP are given in Pack *et al.* (2005).

Input Parameters

The original 7.5 arc seconds (approximately 30.8 m) ASTER DEM grid was resampled to 5 m grid size to produce a finer grid for analysis. Given that the output of the analysis is highly dependent on the quality of the input DEM, the

elevation of the resampled DEM was checked for smoothness and consistency with the mean, maximum and minimum values of the original DEM before implementing in SINMAP.

During the survey, much of the landslide debris runoff was found to be predominantly cohesionless soil, with considerable contents of silt, sand and pumice aggregates. Pumice aggregates as shown in Fig. 8 generally have little cohesive strength and derive most of the shear strength from their high coefficient of friction [tanΦ] due to angularity and interlocking of individual particle. The lower and upper range values of friction angle of the upper layer of the soil considered in the model are therefore 30° and 50°, which are typical for cohesionless soil. Given the dense vegetation of the slopes and the cohesionless nature of the upper soil layer in general, the input lower and upper bound values of both the root and soil cohesions [C_r and C_s respectively] are assumed as 0 kPa and 15 kPa. Based on Eq. 4, the dimensionless cohesion [C] computed is between 0 and 0.85. The saturated soil density [ρ_s] is assumed as 1500 kg/m^3, which is at the lower range of typical values for cohesionless soil, considering the presence of lightweight pumice aggregates.

[Insert Fig. 8 about here]

Based on the rainfall data as shown in Fig 6, the lower and upper bound recharge [R] prior to the earthquake are 43.97 and 56.09 mm/day respectively. Considering the presence of porous pumice aggregates in the silty sand, the hydraulic conductivity of the soil [k] is taken to be between 1×10^{-4} m/s and 1×10^{-5} m/s. The transmissivity [$T=k\times s$] for a layer of 2 m thickness of soil above the failure surface [s] is hence between 1.728 m^2/day and 17.28 m^2/day. With the computed R and T values, the T/R matrix is tabulated as shown in Table 3, which produces a T/R_{min} *and* T/R_{max} of 30.8 m and 393.01 m respectively.

Table 3 Matrix of relative wetness index, T/R

T/R values with:	T_{min}	T_{max}
R_{min}	39.30	393.01
R_{max}	30.81	308.08

Using the above input values of cohesion [C], topographic relative wetness [T/R], friction angle [Φ] and saturated soil density [ρ_s], the contribution area and stability index maps were produced as shown in Figs. 9 and 10.

[Insert Fig. 9 and 10 about here]

Based on Fig. 9, it is apparent that the landslides shown in the satellite image are mainly located at the high contribution streams (denoted as dark blue lines) where rainwater hydrologically converges to these lines and flows to the foot of the slope. The soil in these areas is therefore expected to have a higher degree of saturation which implies a lower effective stress to resist sliding. However, the contribution streams merely indicate the convergence of water flows and are not sufficient to identify the risk of landslide due to the omission of slope stability computation in them. This is supported by the absence of landslides despite the presence of several contribution streams at the right hand side of Fig. 9. As such the slope stability analysis was carried out as shown in Fig. 10. In the slope stability analysis, the areas of highly unstable slopes are indicated in red zones with low stability index (SI

< 1). At areas in the SI map where there are no significant red zones (especially at the right hand side of Fig. 10), large landslides are not visible in the overlaid satellite image. The combination of analysis from contribution streams (Fig. 9) and slope stability analysis (Fig. 10) would give a much accurate identification of areas susceptible to landslide. Locations of Landslides *I* and *II* are indicated in Figs. 9 and 10. Landslide *II* is sited near a high contribution stream (Fig. 9) and unstable slope area (Fig. 10) which substantiates the reliability of the analysis to identify potential areas susceptible to landslides. In the case of Landslide *I*, it is not located near high contribution streams (dark blue lines) and very unstable slope area (dark red zones) as shown in Figs. 9 and 10 respectively. Hence, its occurrence was not expected based on the analysis. On the other hand, there are occasions where areas with low SI values (indicated by dark red zones) did not fail in this earthquake event, implying that the produced SI map is conservative in those areas. The slight inconsistencies in identifying landslide susceptible areas could possibly be due to three reasons: 1) the inaccuracy of elevation interpolation in the resampled DEM at these areas, 2) variability of soil condition, or 3) the effect of strong earthquake leading to variation in reduction of slope stability. High pore water pressure generation (i.e. soil liquefaction) near the soil surface due to the earthquake shaking could have enhanced the landslide occurrence probability. The presence of lightweight pumice aggregates might have also aggravated the problem. Based on field observations, these pumice deposits appeared not extensively cemented but only undergone some compaction under their own weight. In addition, the porous nature of the pumice aggregates allowed rainwater to infiltrate through this upper layer of soil, but the rainwater could not infiltrate further into the deeper, low permeability layers which might have created a film of water beneath the pumice layer where the potential slip failure occurred. High velocity landslide flow could therefore be triggered instantly at regions of near-unstable soil when sheared by the earthquake shaking. Nevertheless, the analysis conducted was capable of identifying large scale landslides which are more likely to result in high property and human losses. Based on the landslide hazard map in Fig. 2, the region is located in the moderate risk zone. However, the occurrence of massive landslides in this region has portrayed that the map is not sufficient. The analysis carried out in this paper has shown to be more capable of identifying areas of high risk of landslides and at a much detailed scale. Despite the success of the analysis, further enhancement to the existing methodology of this analysis to better reflect the effects of earthquake is desirable in the future. Given the frequent occurrence of large earthquakes accompanied with the risk of landslides due to heavy tropical rainfall intensity and soil condition in West Sumatra, it is imperative that the region be reviewed for potential combined effects of rainfall and earthquake which could possibly lead to a revision of the existing landslide risk in some areas of the affected region.

Conclusion

Widespread landslides were triggered in the Padang Pariaman regency and elsewhere during the September 30, 2009 Padang earthquake. The high lethality of these landslides clearly indicates that massive landslides could occur unexpectedly and without warning. A post-earthquake field survey by the UK Earthquake Engineering Field Investigation Team (EEFIT) was conducted at some of these major landslide sites. GPS readings were taken while ascending these landslides and compared with various DEMs overlaid with a SPOT-5 satellite imagery. Results indicate that these data sources gave fairly accurate spatial measurement (latitudinal and longitudinal) of the boundaries of these landslides. The elevation data obtained from these sources differs more considerably. However, the accuracy of these data is still reasonably reliable and does not hamper the analysis of large scale landslides in this

region as portrayed in the deterministic slope stability model with SINMAP. The landslides occurring within the studied region typically fell within the highly unstable zones identified by the analysis, indicating that such stability maps commonly used for rainfall induced landslide assessments are capable of identifying key areas of landslide risk including earthquake induced landslides. There are however occasions where the stability index map gave indication of low landslide risk in areas where landslides were triggered by the earthquake. This could possibly be due to three reasons: 1) the inaccuracy of elevation interpolation in the resampled DEM at these areas, 2) variability of soil condition, or 3) the effect of strong earthquake leading to variation in reduction of slope stability. Pumice aggregates at the upper layer of these slopes might have contributed to the higher susceptibility of landslides due to its low unit density, low cohesion and highly porous nature. Despite the severity of landslides during this earthquake event, this region was demarcated as moderate risk in the local landslide risk map developed in 2010. A review of potential landslide risks considering the effects of earthquakes and proximity may have to be taken into account in addition to the conventional rainfall induced landslide susceptibility studies for Western Sumatra.

Acknowledgement

The authors would like to express their thanks to the Engineering and Physical Sciences Research Council (EPSRC), the Institution of Structural Engineers (IStructE) and the committee and staff of the Earthquake Engineering Field Investigation Team (EEFIT) for their financial and background support for the reconnaissance mission. The provisions of the rainfall data from the Tropical Rainfall Measurement Mission (TRMM) of the National Aeronautics and Space Administration (NASA) and the Japan Aerospace Exploration Agency (JAXA), the SPOT-5 imagery from the Centre for Remote Imaging, Sensing and Processing at the University of Singapore (CRISP NUS), and the ASTER DEM from the National Aeronautics and Space Administration (NASA) are greatly appreciated. The authors are also thankful of the comradeship of John Alarcon, Rini Mulyani and Jessica Whittle during the reconnaissance. This paper is dedicated to the victims of the landslide in Cumanak Village with hopes of providing an account and assessment of the terrible incidents that occurred in the area on the 30th September 2009 and act as a motivator to reduce the incidence of such tragic events in the future.

References

Badan Nasional Penanggulangan Bencana, BNPB (2009) Daily report of the Indonesian National Board for Disaster Management BNPB for the week of 19 October 2009 (In Indonesian), Jakarta

Cruden DM, Varnes DJ (1996) Landslide types and processes. In: Turner AK, Schuster RL (eds) Landslides: Investigations and Mitigation, Chapter 3. Transportation Research Board, Special Report 247, pp 36-75

Emergency Events Database, EM-DAT (2013) Centre for Research on the Epidemiology of Disasters (CRED), Disaster Lists: Earthquake (seismic activity), Tsunami, 26/12/2004. EM-DAT Website http://www.emdat.be/database. Accessed 24 January 2013

Free M, Rossetto T, Peiris N, Taucer F, Zhao N, Koo R, Wang J, Ma X, Verrucci E (2008) The Wenchuan, China Earthquake of 12 May 2008. Earthquake Engineering Field Investigation Team (EEFIT) Preliminary Field Report, The Institution of Structural Engineers, London

Hammond C, Hall D, Miller S, Swetik P (1992) Level I Stability Analysis (LISA) Documentation for Version 2.0. General Technical Report INT-285, USDA Forest Service Intermountain Research Station, Colorado

Irsyam M, Dangkua DT, Hendriyawan, Hoedajanto D, Hutapea BM, Kertapati EK, Boen T, Petersen MD (2008) Proposed seismic hazard maps of Sumatra and Java Island and microzonation study of Jakarta City, Indonesia. J Earth Sys Sci 117(2): 865-878

Natawidjaja DH (2002) Neotectonics of the Sumatran Fault and paleogeodesy of the Sumatran Subduction. PhD Thesis, California Institute of Technology

Pack RT, Tarboton DG, Goodwin CN, Prasad A (2005) A stability index approach to terrain stability hazard mapping: SINMAP user's manual. Utah State University

Petersen M, Harmsen S, Mueller C, Haller K, Dewey J, Luco N, Crone A, Lidke D, Rukstales K (2007) Documentation for the Southeast Asia seismic hazard maps. United States Geological Survey Administrative Report, Virginia

Office for the Coordination of Humanitarian Affairs, OCHA (2009) Indonesia - Earthquake situation report No.8, 7 October 2009. United Nations, New York

Slingerland RL, Voight B (1979) Occurrences, properties, and predictive models of landslide-generated water waves. In: Voight B (ed) Developments in Geotechnical Engineering 14B: Rockslides and Avalanches, 2, Engineering Sites., Elsevier, New York, pp 317–397

United States Geological Survey, USGS (2010a) World earthquake report: Magnitude 7.6 – Southern Sumatra, Indonesia. USGS Website http://earthquake.usgs.gov/earthquakes/eqinthenews/2009/us2009mebz. Accessed 02 February 2013

United States Geological Survey, USGS (2010b) World earthquake report: Magnitude 6.6 – Southern Sumatra, Indonesia. USGS Website http://earthquake.usgs.gov/earthquakes/recenteqsww/Quakes/us2009mfaf.php. Accessed 02 February 2013

Wilkinson SM, Alarcon JE, Mulyani R, Whittle J, Chian SC (2010) The Padang, Sumatra – Indonesia earthquake of 30 September 2009. Earthquake Engineering Field Investigation Team (EEFIT) Field Report, The Institution of Structural Engineers, London

Fig. 1 Locations of earthquake epicentres and fault lines plotted on Google™ Earth background

Fig. 2 Regency (and city) level landslide risk map for Sumatera Barat (West Sumatra) province, as of 08 February 2010 (Source: Indonesian National Board for Disaster Management, BNPB)

Fig. 3 Location of major landslides (in crosses), spatial distribution of human casualties and building damage (BNPB 2009) and Modified Mercalli Intensity scale isoseismal lines (USGS 2010a) in the affected regencies of Sumatera Barat province, plotted on Google™ Earth background

Fig. 4 3-hourly rainfall measurements in Padang during the month of September 2009, UTC time (Source: Tropical Rainfall Measurement Mission, TRMM)

Fig. 5 View of a slip-circle landslide failure at Pulau Air Village (seen from the crest of the landslide)

Fig. 6 View of an infinite slope landslide failure at Cumanak Village from near the summit of the landslide

(a) Landslide *I* (0^{o}29'54.64"S 100^{o}14'26.59"E) (b) Landslide *II* (0^{o}29'54.64"S 100^{o}14'26.59"E)

Fig. 7 Locations of landslide boundary points, superimposed on SPOT-5 image acquired by CRISP NUS with Google™ Earth's terrain background feature

Fig. 8 Weathered pumice observed on the surface of the investigated landslide debris

Fig. 9 Contribution area map overlaid with SPOT-5 satellite image from CRISP NUS

Fig. 10 Stability index (SI) map overlaid with SPOT-5 satellite image from CRISP NUS

Figure 1
Click here to download high resolution image

Figure 2
Click here to download high resolution image

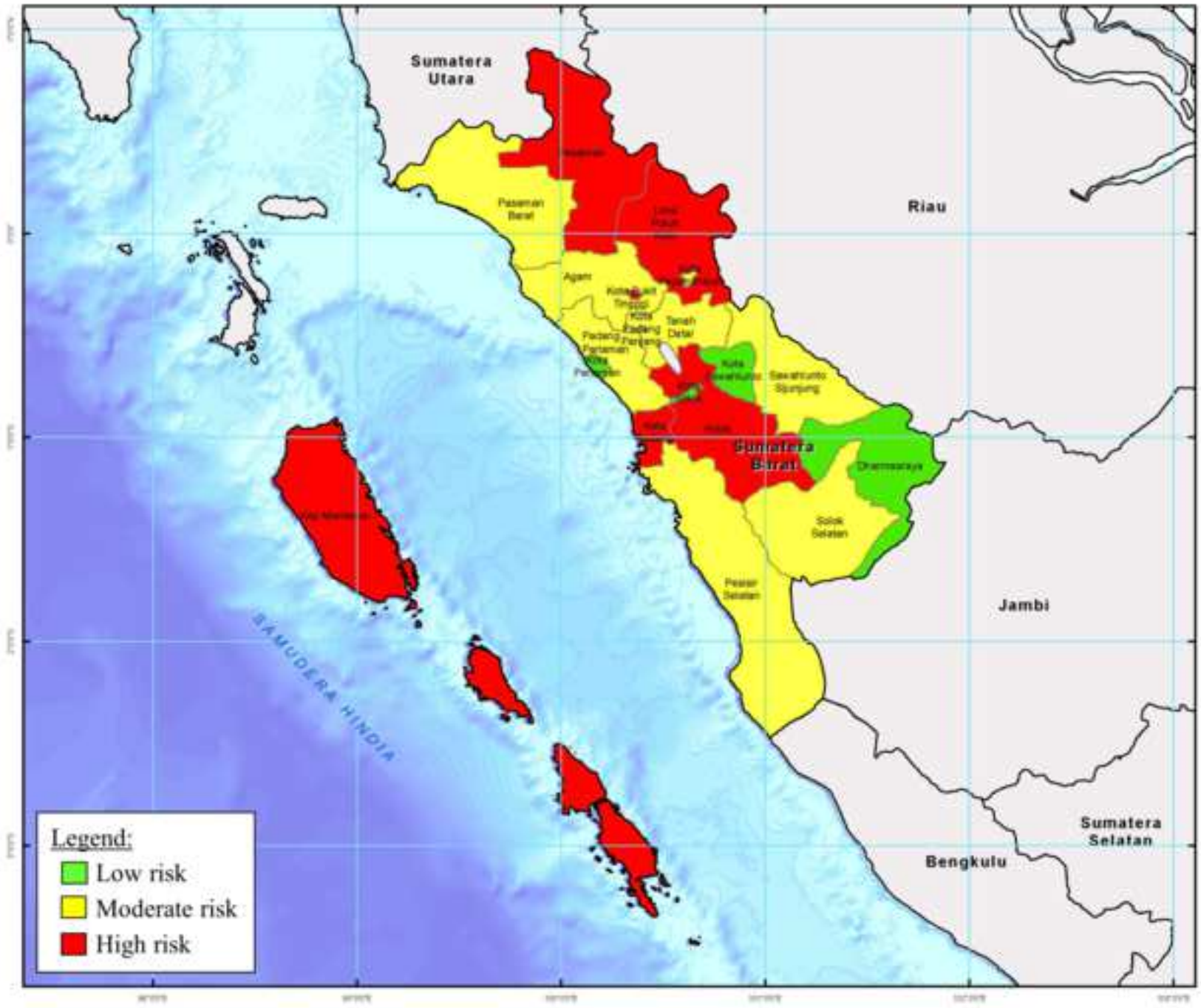

Figure 3
Click here to download high resolution image

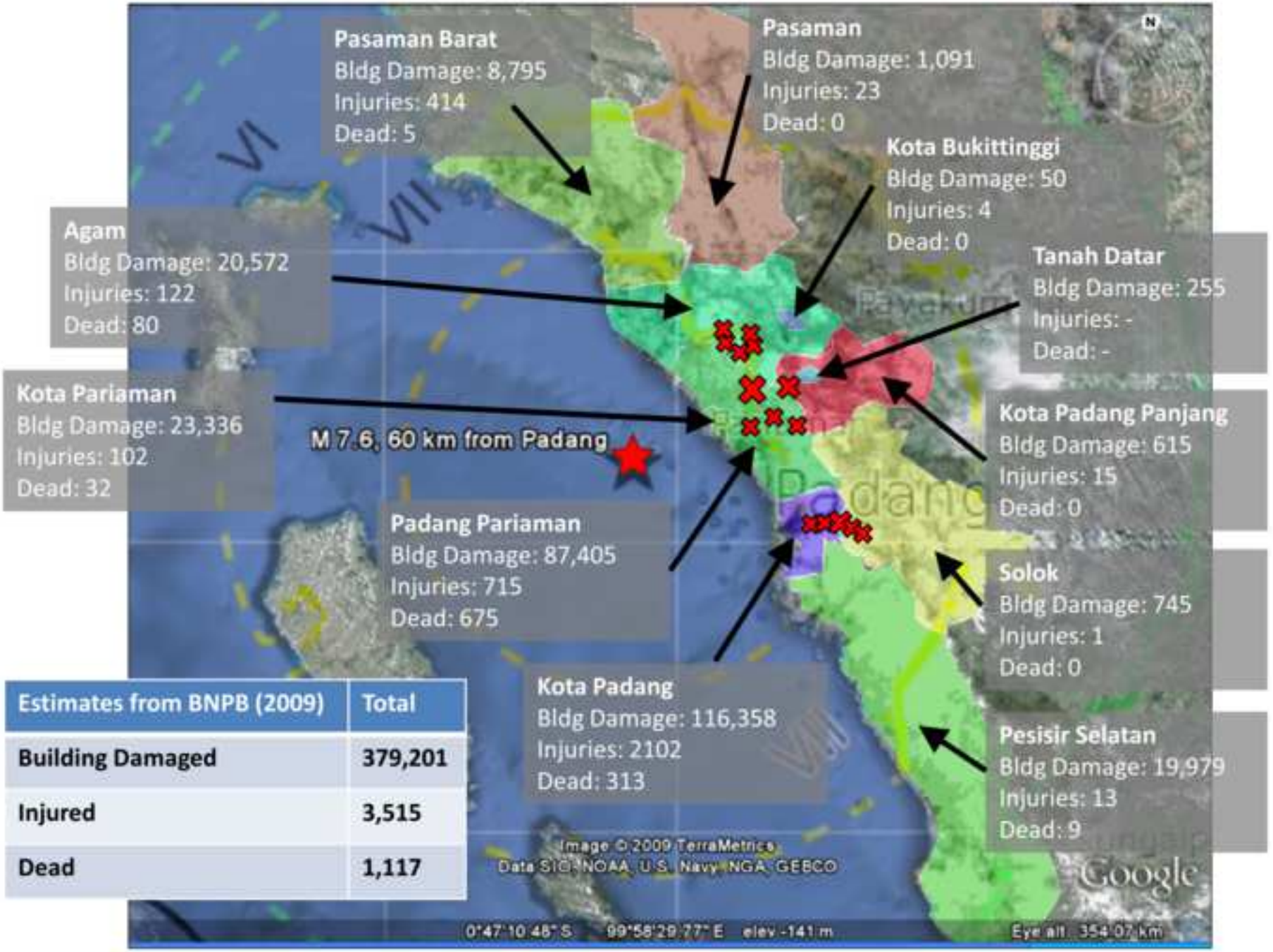

Estimates from BNPB (2009)	Total
Building Damaged	379,201
Injured	3,515
Dead	1,117

Figure 4
Click here to download high resolution image

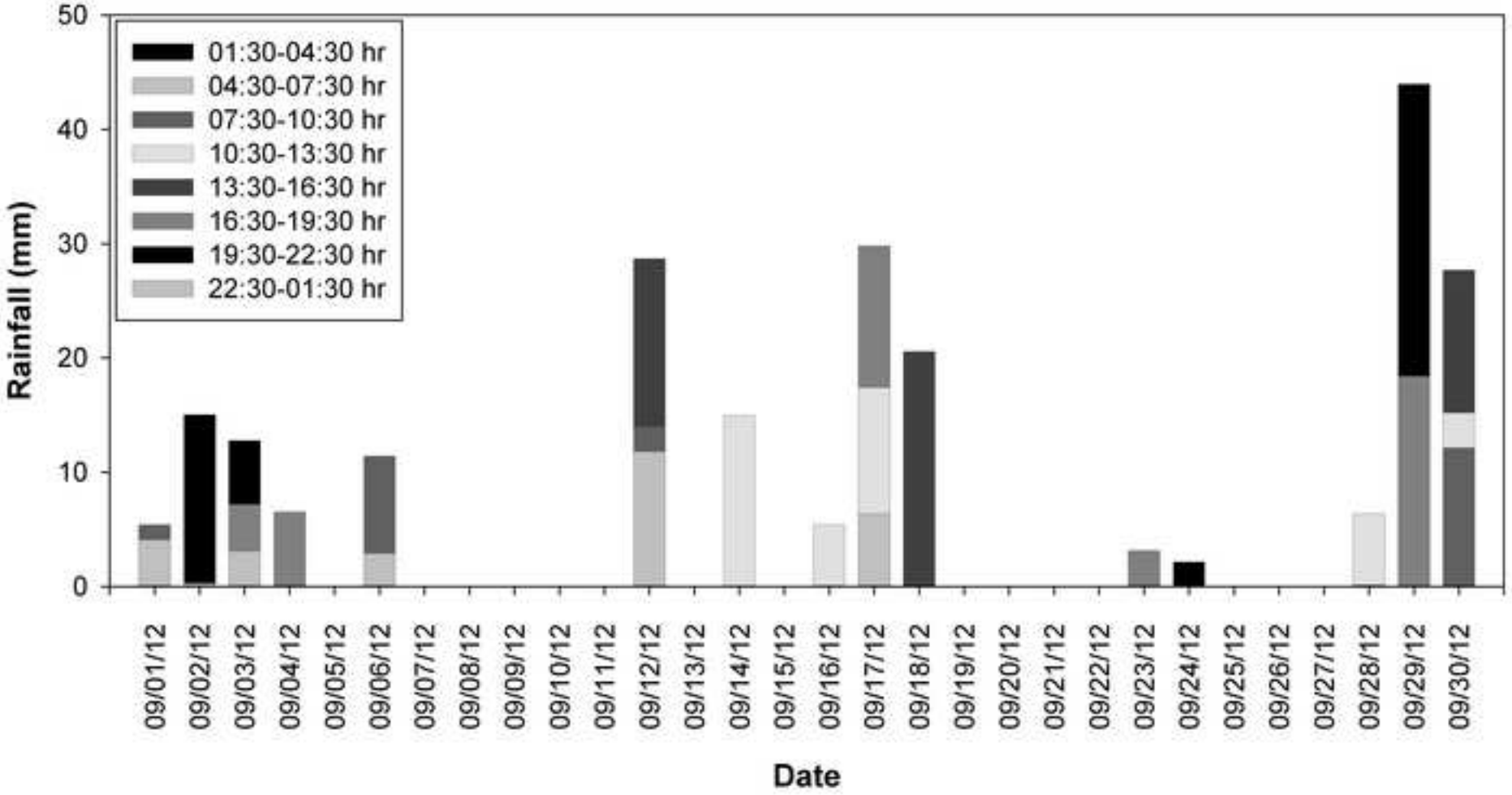

Figure 5
Click here to download high resolution image

Figure 6
Click here to download high resolution image

Figure 7a
Click here to download high resolution image

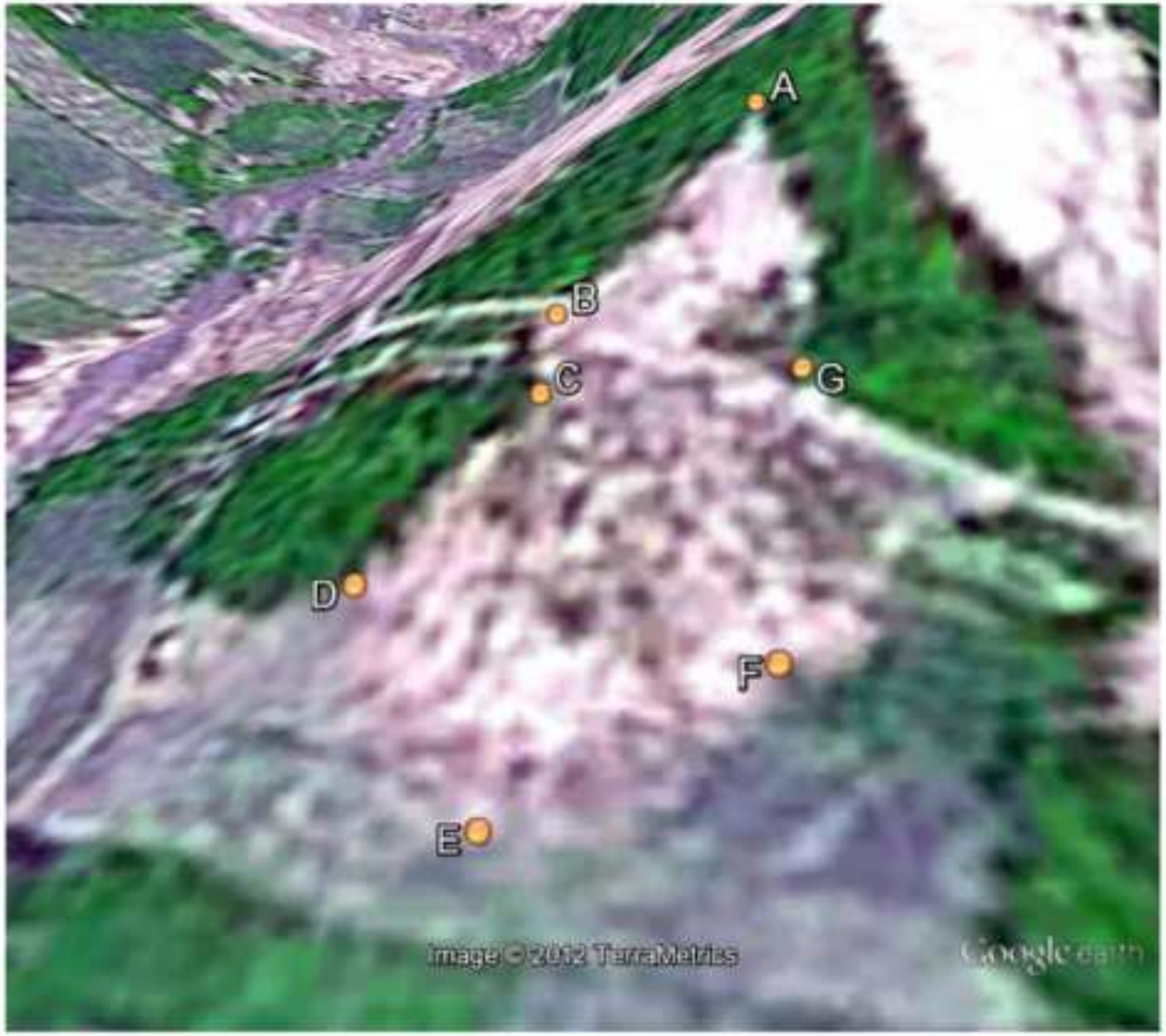

Figure 7b

Click here to download high resolution image

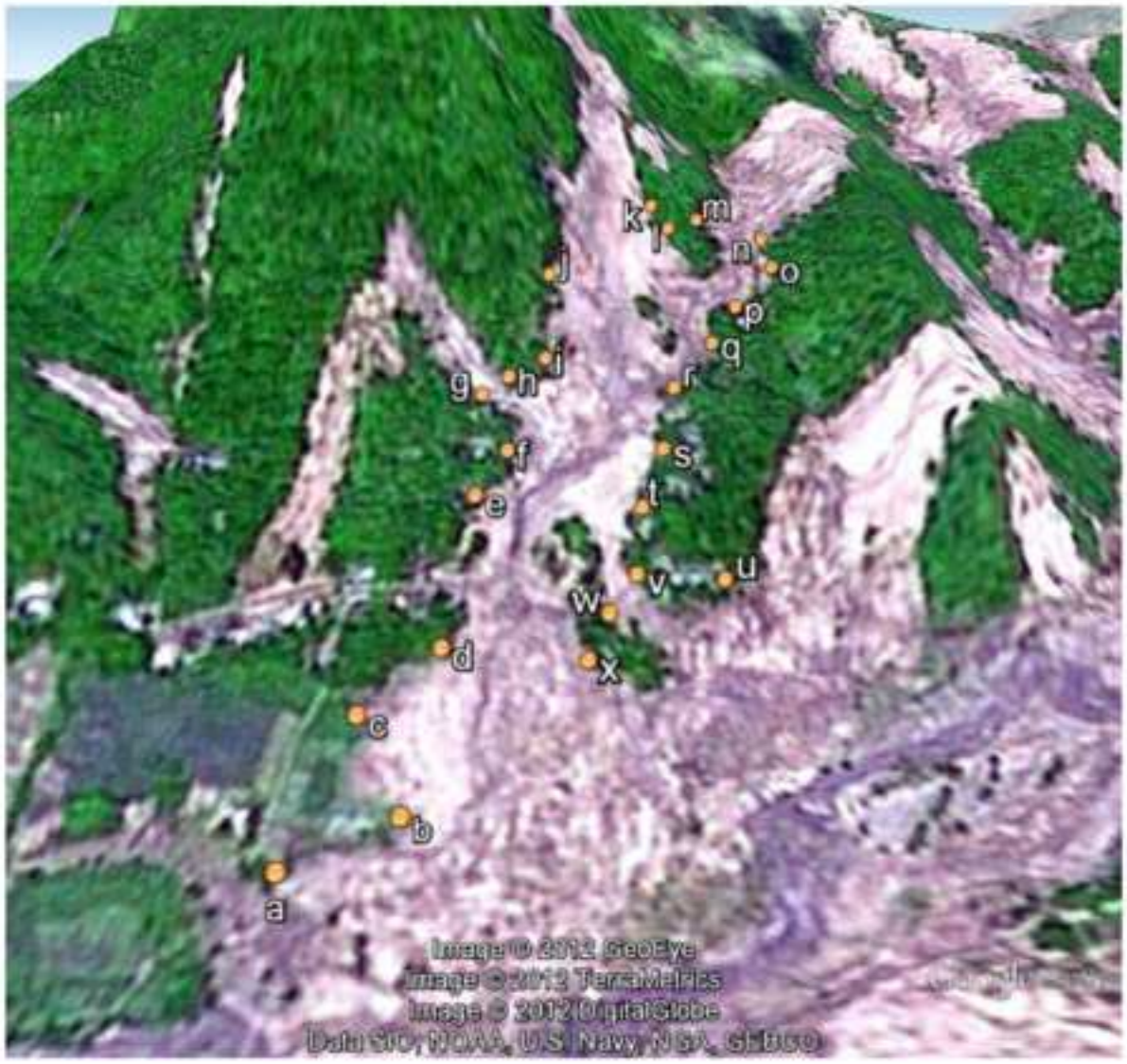

Figure 8
Click here to download high resolution image

Figure 9
Click here to download high resolution image

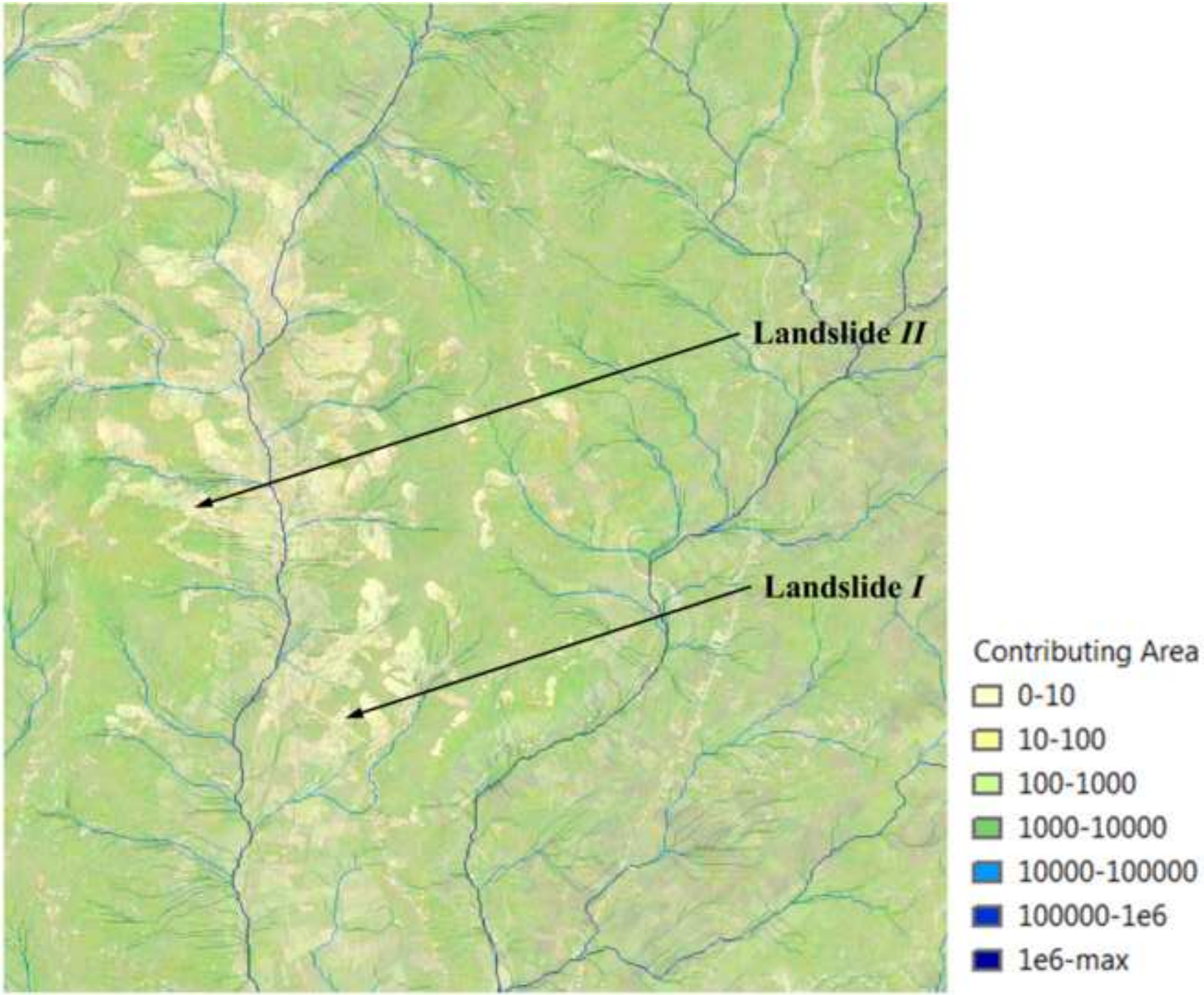

Figure 10
Click here to download high resolution image